Chemical Science

ROYAL SOCIETY OF CHEMISTRY

EDGE ARTICLE

View Article Online
View Journal | View Issue

Cite this: *Chem. Sci.*, 2026, **17**, 4213

All publication charges for this article have been paid for by the Royal Society of Chemistry

Modulation of nanoscale sinuosity in asymmetric nano-channels for high-resolution separation of trace xylene isomer impurities

Ming Xu, † Xiao-Yi Fu,† Sha-Sha Meng,† Shu-Rui Gao, Yu Wang and Zhi-Yuan Gu *

Received 1st October 2025
Accepted 26th December 2025

DOI: 10.1039/d5sc07611k

rsc.li/chemical-science

The purification of *para*-xylene (*p*X) to ultra-high levels is critical for producing high-performance polyethylene terephthalate, yet trace-level quantification of its isomeric impurities, *meta*-xylene (*m*X) and *ortho*-xylene (*o*X), remains a formidable challenge due to their nearly identical boiling points and molecular dimensions. This study presents an aluminum-based metal–organic framework, Al-TCPB-Me_2, featuring asymmetric one-dimensional channels with a high sinuosity ratio that coupled molecular sieving and shape matching to achieve the baseline separation of xylene isomers. Structural characterization confirmed a sinuous channel with an entrance size of ~6.8 Å, which excluded *o*X while enabling selective recognition of *p*X over *m*X through asymmetric binding sites. Density functional theory calculations revealed that four methyl groups in the sinuous channel formed hydrophobic interactions with two methyl groups in *p*X molecules, while only three methyl groups interacted with methyl groups in *m*X molecules, resulting in stronger binding of *p*X than *m*X. The Al-TCPB-Me_2 column achieved high separation resolutions (24.9 for *m*X/*p*X and 31.1 for *o*X/*p*X) and successfully quantified the impurities as low as 200 ppm in the real high-quality xylene sample, surpassing all conventional columns. Comparative tests with a straight-channel Al-TCPB variant emphasized the sinuous geometry's role in enabling tandem separation mechanisms. This work establishes asymmetric sinuous channels as an effective design principle for integrating tandem molecular sieving and shape matching, offering a powerful strategy for the quantification of trace-level structurally similar impurities in real sample analysis.

Introduction

para-Xylene (*p*X) is a crucial precursor in the production of terephthalic acid (PTA), which is essential for manufacturing polyethylene terephthalate (PET) plastics and polyester fibers widely used in packaging, textiles, and consumer goods.[1–3] The production of high-performance polyester requires ultra-high-purity *p*X, placing stringent demands on the detection and quantification of impurities, particularly its isomeric counterparts. *meta*-Xylene (*m*X) and *ortho*-xylene (*o*X) are the primary isomeric impurities, and even trace amounts of them can adversely affect the properties and performance of downstream products.[4] However, the quantification of impurities in *p*X presents severe analytical challenges, which arises from the isomers' minimal boiling point variations (0.7–6.0 K) and similar molecular dimensions (*p*X: 5.8 Å; *m*X: 6.8 Å; *o*X: 6.8 Å).[5,6] Conventional gas chromatography (GC) stationary phases hardly achieve xylene isomer separation due to these physicochemical similarities, leading to compromised accuracy in the quantification of *p*X impurities, especially the isomeric impurities at trace levels.[7,8] This underscores the urgent need for highly selective chromatographic stationary phases with enhanced separation efficiency and accuracy in trace impurity quantification.[9]

Metal–organic frameworks (MOFs) have emerged as promising materials for the separation of structurally similar molecules due to their precisely tunable pore environments.[10–12] Controlling pore architecture has enabled improved separation of aromatic isomers, alkane/alkene mixtures, electronic specialty gases, and cyclohexane/benzene azeotropes in adsorption and chromatographic systems.[13,14] Despite these developments, current MOF-based separators remain insufficient for the analytical demands of industrial *p*X purification. Most reported systems focus on equimolar or simplified binary mixtures and aim to enhance adsorption selectivity under balanced laboratory conditions.[15] However, industrial impurity analysis presents a fundamentally different challenge, where trace-level *m*X and *o*X must be detected in the presence of an overwhelmingly dominant *p*X matrix—often with concentration

State Key Laboratory of Microbial Technology, Jiangsu Collaborative Innovation Center of Biomedical Functional Materials, Jiangsu Key Laboratory of New Power Batteries, College of Chemistry and Materials Science, School of Food Science and Pharmaceutical Engineering, Nanjing Normal University, Nanjing 210023, China. E-mail: guzhiyuan@njnu.edu.cn

† These authors contributed equally to this work.

differences spanning several orders of magnitude. Under such extreme disparity, even MOFs with good inherent selectivity struggle because of competitive adsorption from the dominant component. A fundamentally new material design paradigm is required, one capable of selective recognition of minor impurities despite the intense competitive adsorption from the major component.

Classical separation mechanisms provided by MOF separators alone are insufficient to meet this requirement.[16–21] Molecular sieving selectively adsorbs smaller molecules while excluding larger species,[22–24] whereas shape matching relies on the geometric fit between adsorbates and pore environments to induce strong configuration-specific interactions.[25–29] Recent studies have validated combining molecular sieving and shape matching as an efficient means to further enhance the separation performance of MOFs.[30–32] In practice, however, these approaches have relied predominantly on size-based sieving, while the potential of shape matching has been less fully realized. In most cases, shape matching merely reinforces sieving or enhances adsorption capacity, rather than directly separating molecules after adsorption.[13,14] This limitation arises largely from the prevailing use of symmetric channel architectures, in which separation is achieved by tuning channel windows to exclude larger molecules (Scheme 1a). Such an approach makes it difficult to modify the internal cavity geometry and thus restricts the precision of shape matching.[30,31] From a geometric standpoint, asymmetric channels present a more versatile alternative because they are inherently sensitive to subtle differences in molecular geometry and provide greater opportunities for coupling sieving with shape recognition.[33–35] Importantly, asymmetry can be introduced through chemical functionalization, which not only regulates channel window size but also modifies channel sinuosity, thereby enabling more precise discrimination of structural isomers (Scheme 1b). The sinuosity ratio (SR) of MOF channels can be defined analogously to the river sinuosity ratio, where SR values below 1.1 indicate straight channels and values above 1.1 indicate sinuous channels (Fig. S1). Applying this principle to the particularly demanding separation of xylene isomers requires delicate channel design, in which both asymmetry and sinuosity are finely tuned to achieve optimal molecular complementarity.

Herein, to construct the asymmetric sinuous channels, $Al(OH)_2O_4$ chains with zigzag coordination mode and TCPB-Me_2 (H_4TCPB-Me_2 = 1,2,4,5-tetrakis(4-carboxyphenyl)-3,6-dimethyl-benzene) with two additional methyl groups as constraints were chosen to coordinate in a staggered manner. It was then developed as a high-performance stationary phase for baseline separation of trace xylene isomers from their main component through the synergistic molecular sieving and shape-matching mechanisms. The powder X-ray diffraction (PXRD) pattern and high-angle annular dark-field (HAADF) image confirmed that the Al-TCPB-Me_2 framework possessed an ***frl*** topology with a one-dimensional (1D) sinuous channel (channel 1, SR = 1.14, Fig. 1) with the entrance size of approximately 6.8 Å. *o*X with the largest size was excluded from channel 1 and exhibited the fastest diffusion constant among the three isomers. At the same time, the sinuous geometry resulted in asymmetric binding sites inside the channel, leading to different shape-matching effects for *p*X and *m*X. Density functional theory (DFT) simulations demonstrated that *p*X exhibited the strongest binding energy to the channel.[36,37] In detail, the alignment of the four methyl groups in the channel interacted with the two methyl groups in *p*X molecules, while only three methyl groups interacted with the two methyl groups in *m*X molecules, resulting in more negative binding energies of *p*X than *m*X. Moreover, the Al-TCPB-Me_2 stationary phase achieved the separation resolution (R_s) values of 24.9 and 31.1 for *m*X/*p*X and *o*X/*p*X, respectively, which were much higher than those of the commercial column HP-5. Most importantly, the Al-

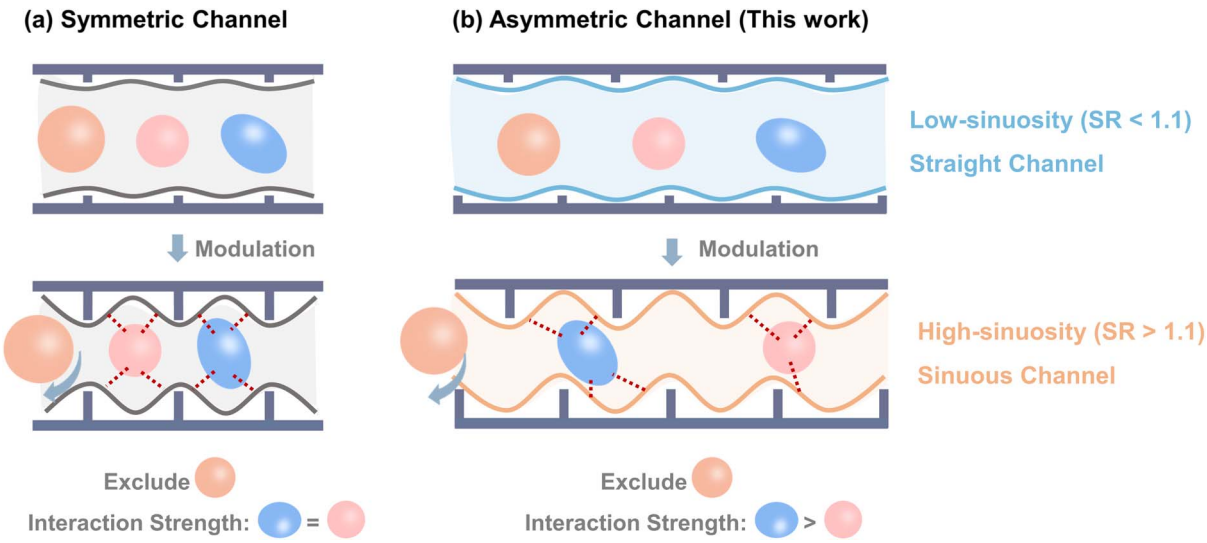

Scheme 1 (a) The schematics of modulating the symmetric channel to combine molecular sieving and shape matching mechanisms. (b) The schematics of modulating the asymmetric channel sinuosity to combine molecular sieving and shape matching mechanisms in this work. The sinuosity ratio (SR) lower than 1.1 indicates a straight channel, while SR higher than 1.1 indicates a sinuous channel.

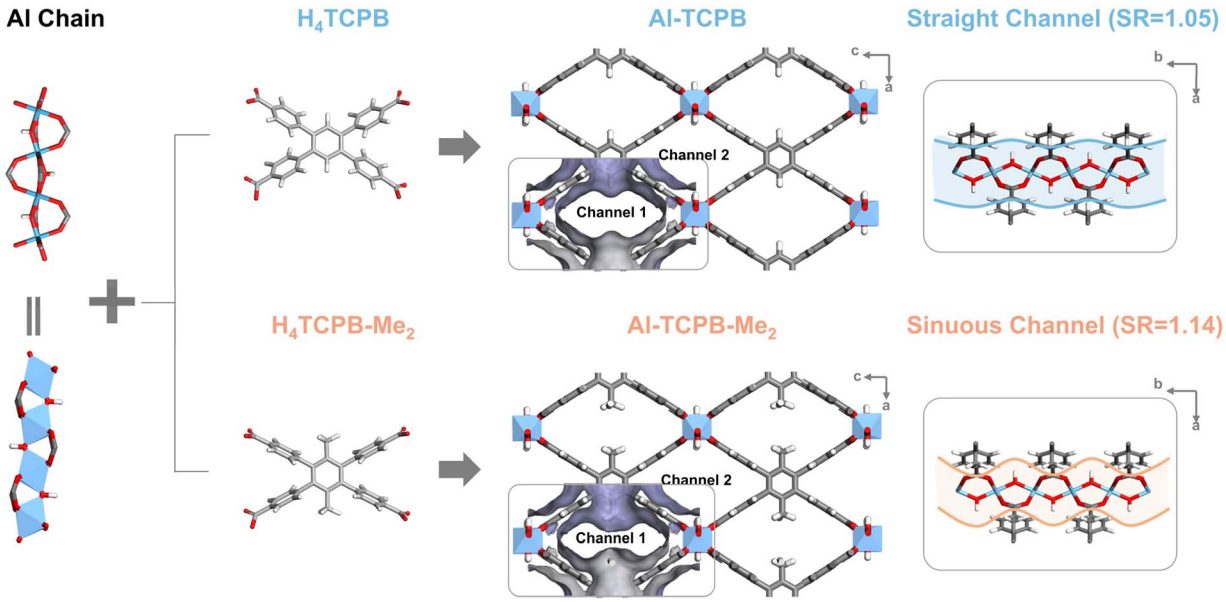

Fig. 1 Schematic illustration of isostructural Al-TCPB and Al-TCPB-Me_2 MOFs constructed from aluminium chains and H_4TCPB/H_4TCPB-Me_2 ligands. These two MOFs contain two types of channels, the sinuous/straight channel 1 and the straight channel 2. The figures in the rightmost column highlight the side view of channel 1 from the *c*-axis.

TCPB-Me_2 column can quantify the trace *m*X or *o*X isomer impurities at concentrations as low as 200 ppm in the pure *p*X sample. For comparison, an Al-TCPB stationary phase with straight channel 1 (SR = 1.05) was also developed.[38] Although Al-TCPB demonstrated good performance in separating the *para*-isomer from chlorotoluene and dichlorobenzene, it failed to separate *meta*- and *ortho*-isomers, highlighting the crucial role of the asymmetric sinuous channel in providing tandem separation mechanisms and achieving superior separation performance. This work not only presented promising materials for the qualification of trace-level xylene impurity but also provided an effective design strategy for the development of separators with tandem separation mechanisms for challenging multi-component separations.

Results and discussion

Synthesis and characterization

The MOF Al-TCPB was synthesized through a one-pot method, and Al-TCPB-Me_2 was obtained in a similar manner but by changing the ligand from H_4TCPB to H_4TCPB-Me_2. The ^{1}H nuclear magnetic resonance (NMR) spectra proved the structures of the two ligands (Fig. S2). The reported structural data revealed that the Al-TCPB framework adopts the ***frl*** topology, with the 3D coordination network consisting of infinite 1D $Al(OH)_2O_4$ chains and tetratopic carboxylic acid ligands.[38] In the 1D $Al(OH)_2O_4$ chains, the aluminum ions exhibit an octahedral coordination environment, with two μ-OH groups and four carboxyl oxygen atoms from four distinct ligands participating in the coordination. The ligands coordinated with $Al(OH)_2O_4$ chains in a staggered manner along the *b*-axis, forming two types of 1D channels, referred to as channel 1 and channel 2 (Fig. 1). Channel 2 is a completely straight channel in which four benzene rings are oriented toward the pore interior, while channel 1 is nearly straight but exhibits slight sinuosity due to the presence of hydrogen atoms on the asymmetric organic ligands. The SR of Al-TCPB channel 1 was calculated as 1.05, confirming that it can reasonably be regarded as a straight channel in the subsequent discussion. The powder X-ray diffraction (PXRD) pattern of the synthesized Al-TCPB was recorded to confirm its structure and crystallinity. The sharp diffraction peaks of Al-TCPB showed minimal deviation from the simulated one, confirming its high crystallinity and the ***frl*** topology (Fig. 2a). The diffraction peaks at 5.23°, 8.00°, and 9.70° correspond to the (001), (200), and (201) planes of the Al-TCPB structure.

Although the structural data for Al-TCPB-Me_2 has not yet been reported, we hypothesized that Al-TCPB-Me_2 shared an identical topology with Al-TCPB, with the only difference being the organic ligands. The introduction of additional methyl groups as constraints increased the sinuosity of channel 1 as well as functionalized the asymmetric methyl sites (Fig. 1). Consequently, the SR of channel 1 increased from 1.05 to 1.14, indicating the formation of an asymmetric sinuous channel in Al-TCPB-Me_2. The solid-state ^{13}C NMR spectra proved the presence of two methyl groups in the synthesized Al-TCPB-Me_2 (Fig. S3). Al-TCPB-Me_2 exhibited almost identical PXRD patterns to the simulated Al-TCPB, supporting their structural similarity. Notably, the diffraction peak for the (200) plane shifted from 8.00° to 9.29°, likely due to the introduction of the methyl groups, which reduced the interplanar spacing.[39,40] Furthermore, the diffraction peaks of Al-TCPB-Me_2 were broader compared to those of the synthesized Al-TCPB, suggesting relatively lower crystallinity.[41,42]

The scanning electron microscopy (SEM) images showed that Al-TCPB-Me_2 possessed nanoplate morphology (Fig. S4). In

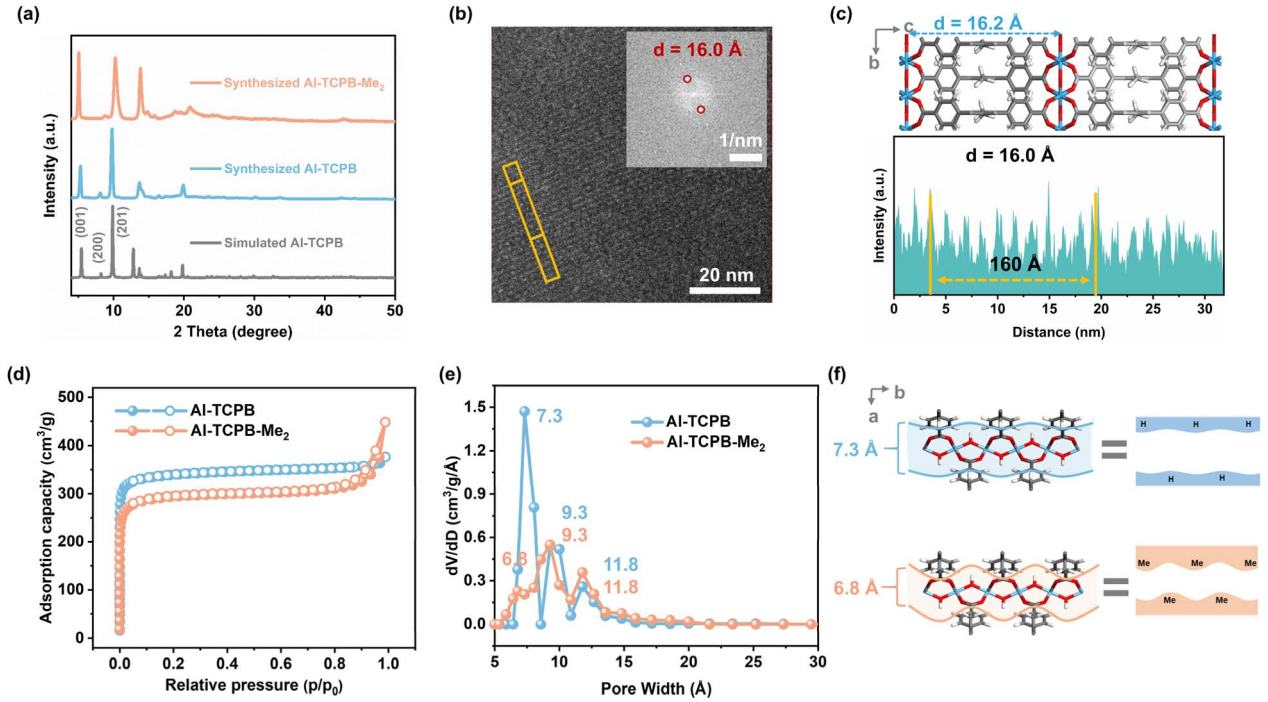

Fig. 2 (a) The PXRD patterns of Al-TCPB and Al-TCPB-Me_2. (b) The original HAADF image of Al-TCPB-Me_2. The insert shows its FFT pattern. The *d*-spacing of two diffraction points was measured as 16.0 Å. (c) The structure of Al-TCPB-Me_2 viewed from the *a*-axis and the intensity profile along the orange area in (b). (d) The N_2 adsorption–desorption isotherms and (e) the pore size distributions of Al-TCPB and Al-TCPB-Me_2. (f) Channel size comparison between Al-TCPB and Al-TCPB-Me_2.

order to investigate the topology of Al-TCPB-Me_2, high-angle annular dark-field (HAADF) imaging was performed. The HAADF images revealed distinct lattice fringes (Fig. 2b), in which the Al chains were distinguishable as white lines against the background and other nonmetallic atoms. The simulated structure of Al-TCPB-Me_2 viewed from the *a*-axis indicated that the interspacing between Al chains was 16.2 Å (Fig. 2c). The intensity profiles along the highlighted orange area in the HAADF image exhibited a spacing of 16.0 Å between Al chains, which coincides with the simulated interplanar spacing of the (001) plane. In addition, the calculated *d*-spacing of two adjacent points in the fast Fourier transform (FFT) pattern was also 16.0 Å, which was consistent with the interplanar spacing (16.2 Å) of the (001) plane. The above experimental findings further confirmed that Al-TCPB-Me_2 has the same structure as Al-TCPB.

The N_2 adsorption analysis was employed to analyze the pore structures of the two Al-MOFs (Fig. 2d). Both materials displayed type-I isotherms and steep slopes at ultra-low pressures, indicating the presence of intrinsic micropores and a strong binding affinity between N_2 molecules and the MOF channels. The N_2 adsorption capacity ($p/p_0 = 0.8$) of Al-TCPB-Me_2 (312 cm^3 g^{-1}) was slightly lower than that of Al-TCPB (353 cm^3 g^{-1}). Similarly, the BET surface area of Al-TCPB-Me_2 (1141 m^2 g^{-1}) was smaller than that of Al-TCPB (1331 m^2 g^{-1}). These differences were attributed to the introduction of asymmetric methyl groups, which slightly changed the pore structure and hindered the N_2 adsorption. The pore size distribution, calculated using the H–K (Saito–Foley) method, revealed that both Al-MOFs contained three distinct pores (Fig. 2e). Both Al-TCPB and Al-TCPB-Me_2 had two types of pores with similar dimensions of 9.3 Å and 11.8 Å, respectively (Table S1). The smallest pore size shifted from 7.3 Å in Al-TCPB to 6.8 Å in Al-TCPB-Me_2, with a noticeable reduction in the proportion of the smallest pores in Al-TCPB-Me_2 (Fig. 2f). These observations further indicated that the introduction of the asymmetric methyl groups in the ligand partially reduced the pore volume, forming the sinuous channel with a reduction in the size of channel 1. However, the remaining channel 2 was not affected due to the similarity in topology.

The thermal stability of Al-TCPB and Al-TCPB-Me_2 was evaluated by thermogravimetric analysis (TGA) under an oxygen atmosphere (Fig. S5). The results showed that due to differing amounts of residual solvent in the materials, the mass loss of Al-TCPB and Al-TCPB-Me_2 before 250 °C was 5.60% and 3.64%, respectively. The sinuous channel of Al-TCPB-Me_2 adsorbed less residual solvent compared to the straight channel of Al-TCPB. Both host frameworks maintained structural integrity up to 425 °C, indicating the high thermostability of the two Al-MOFs. This stability can be attributed to the strong aluminum–oxygen (Al–O) bonds and the stable coordination between the Al^{3+} center and the carboxylate ligands.

Molecular sieving provided by the asymmetric sinuous channel

After the successful synthesis of the two Al-MOFs with distinct channel architectures, they were measured in the inverse GC

using xylene isomers as model analytes to evaluate the molecular sieving capabilities for isomer differentiation. The SEM images of the MOF-coated 15 meter columns in the cross-sectional view revealed that the dynamic coating process and temperature programming did not affect the morphology of MOFs (Fig. S6). Then, the kinetic parameters, including diffusion constants (D_s) and mass transfer coefficients (C-term) at 230 °C, were calculated for the comparison between Al-TCPB and Al-TCPB-Me_2. Notably, the D_s values and C-terms for *o*X, *m*X, and *p*X showed minimal differences when tested with the Al-TCPB coated column. Similar D_s values and C-terms indicated that Al-TCPB cannot provide the molecular sieving effect to distinguish these isomers. The smallest pore window of Al-TCPB is 7.3 Å, which is still larger than all the xylene isomers, meaning that all the xylene isomers can enter channel 1 and channel 2 of Al-TCPB, resulting in no sieving effect.

When it came to Al-TCPB-Me_2, the phenomenon had changed. *p*X with the smallest kinetic diameter clearly exhibited the smallest D_s and the largest C-terms in the Al-TCPB-Me_2 coated column, indicating the slowest diffusion of *p*X in Al-TCPB-Me_2. This suggested that, unlike Al-TCPB, Al-TCPB-Me_2, with its smallest pore window of 6.8 Å, was able to provide the molecular sieving effect, allowing the smallest *p*X to get into channel 1 while excluding larger isomers. Interestingly, *o*X and *m*X, which have almost identical kinetic diameters, displayed significantly different diffusion behaviors in Al-TCPB-Me_2. The D_s value of *o*X was 2.4 times higher than that of *m*X, indicating that most *o*X molecules likely diffused through the stationary phase without entering the smallest channel 1 (Fig. S7 and Table S2). This behavior resulted from the unique sinuous shape of channel 1. The sinuous channel provided a tilted entrance for *meta*-positioned *m*X molecules, while the methyl group positioned at the channel entrance imposed additional steric hindrance on *o*X molecules with *ortho*-positioned dual methyl groups. During the fast adsorption and desorption processes, the large diffusion barrier prevented most *o*X molecules from entering channel 1, leading to molecular exclusion. Notably, this molecular exclusion of *o*X was weakened during adsorption at thermodynamic equilibrium. Single-component vapor adsorption experiments revealed that *o*X exhibited a slightly higher adsorption capacity in Al-TCPB-Me_2 under saturated conditions, suggesting that *o*X was also able to access channel 1 at high molecular concentrations (Fig. S8). The equilibrium adsorption experiments allowed molecules sufficient time to explore accessible pore spaces. Under these conditions, *o*X might occupy the local adsorption pockets, and its adjacent methyl groups provided a larger hydrophobic contact area, resulting in slightly higher equilibrium uptake than *m*X. It is worth noting that since channel 2 of both Al-TCPB and Al-TCPB-Me_2 was identical and larger than all the xylene isomers, the differing mass transfer behavior of isomers was primarily attributed to the shape of channel 1.

Shape matching with the asymmetric sinuous channel

To further investigate the shape-matching effects provided by the two Al-MOFs, the enthalpy of adsorption (ΔH), entropy of adsorption (ΔS), and Gibbs free energy of adsorption (ΔG) for xylene isomers were calculated. As shown in Fig. S9, the van't Hoff plot exhibited a linear relationship, indicating that the interaction mechanism between the MOFs and adsorbates remained consistent across the temperature range.

For Al-TCPB, the ΔH values followed the order *m*X > *o*X > *p*X ($-70.9 > -72.7 > -73.2$ kJ mol^{-1}, Table S3). *p*X exhibited the most negative ΔH value when tested with the Al-TCPB coated column, although the differences were not pronounced. Thus, *p*X, with the longest molecular length, was able to interact synergistically with both channel walls, leading to a stronger affinity for Al-TCPB. In contrast, *o*X, with two methyl groups in adjacent positions, was reported to interact simultaneously with the metal chains, resulting in intermediate interactions with the backbone.[43] The shape of *m*X allowed it to use only one of its two methyl groups to interact with the channel wall, leading to the weakest interaction. These results suggested that Al-TCPB with a low SR can provide a shape-matching effect to distinguish the thermodynamic differences between the three xylene isomers, although this effect was not significant.

For Al-TCPB-Me_2, the ΔH values for Al-TCPB-Me_2 followed the order *o*X > *m*X > *p*X ($-68.5 > -75.7 > -89.4$ kJ mol^{-1}). The difference in ΔH values was much more significant, indicating that Al-TCPB-Me_2 offered greater distinguishability than Al-TCPB. Notably, the ΔH value for *o*X in Al-TCPB-Me_2 was less negative than in Al-TCPB and also less negative than *p*X and *m*X in Al-TCPB-Me_2, further supporting the speculation that *o*X molecules were predominantly excluded by sinuous channel 1, preventing them from accessing the adsorption sites within channel 1. The ΔH values for *p*X were much more negative than those for *m*X, suggesting a stronger interaction between *p*X and Al-TCPB-Me_2. We supposed that the high sinuosity introduced by asymmetric methyl groups enhanced the shape-matching effect, thereby amplifying the geometric distinctions among xylene isomers. Within the sinuous channels, the methyl groups can closely interact with the linear *p*X molecules, forming the strongest interaction. In contrast, *m*X molecules with *meta*-positioned methyl groups were unable to form the same interactions, resulting in a weaker interaction. The ΔS and ΔG values for the three isomers on Al-TCPB-Me_2 further supported this hypothesis (Table S3). These results proved that the sinuous channels of Al-TCPB-Me_2 can provide an effective shape-matching effect to distinguish isomers.

To test the above hypothesis, density functional theory (DFT) simulations, conducted using VASP software, were employed to further explore the shape-matching phenomena between *p*X and *m*X within the asymmetric sinuous channel 1 of Al-TCPB-Me_2 (see the SI for details). The adsorption positions of *p*X and *m*X molecules within the channel were optimized to minimize the binding energy before the comparison. The final calculated binding energies for *p*X and *m*X were -84.42 kJ mol^{-1} and -75.22 kJ mol^{-1}, respectively. The observed trend in binding energies aligned with the experimental ΔH values obtained from the inverse GC method. As illustrated in Fig. 3d and e, both *p*X and *m*X could form C–H$\cdots\pi$ interactions with the Al-TCPB-Me_2 framework. However, the dual methyl groups of linear *p*X were in closer proximity to the four methyl groups of

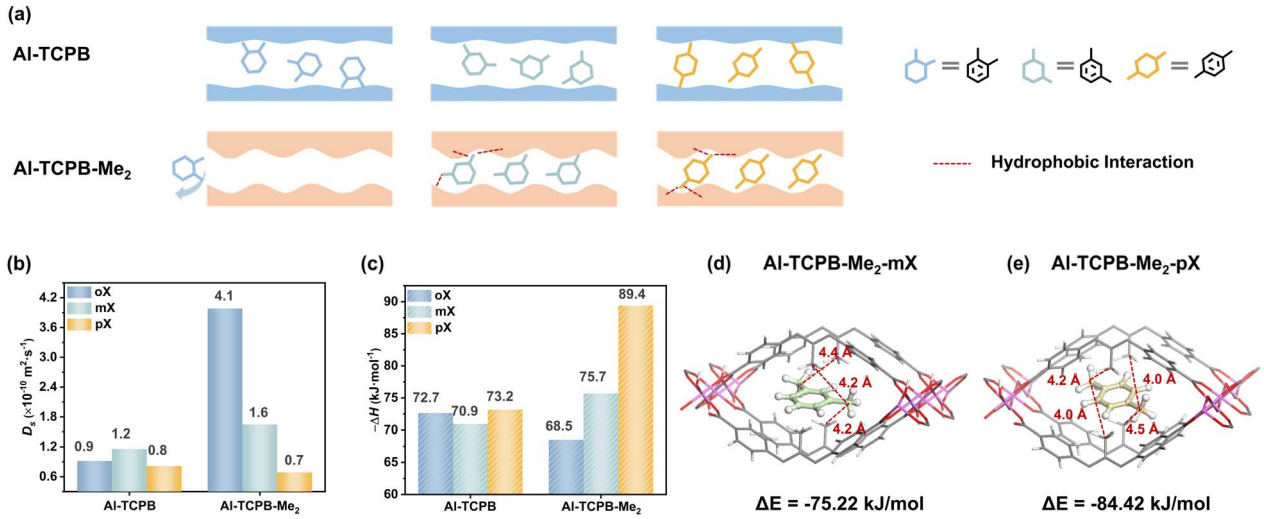

Fig. 3 (a) Schematic diagrams of *o*X, *m*X, and *p*X molecule transport through the asymmetric sinuous channel 1 of Al-TCPB and Al-TCPB-Me_2, respectively. (b) The experimental D_s values of *o*X, *m*X, and *p*X on Al-TCPB and Al-TCPB-Me_2, respectively. (c) The experimental $-\Delta H$ values of *o*X, *m*X, and *p*X on Al-TCPB and Al-TCPB-Me_2, respectively. The DFT calculated locations of (d) *m*X and (e) *p*X within the zigzag pore of Al-TCPB-Me_2, showing the distinguished binding sites and interactions.

the organic ligands, resulting in a more complete hydrophobic contact between its two methyl groups and the densely methyl-decorated channel walls, which maximized dispersive interactions. In contrast, the *m*X molecule was shorter, and its *meta*-positioned methyl groups interacted with only three methyl groups of the organic ligands, leading to an incomplete overlap with these hydrophobic regions. Thus, the asymmetric sinuous channel amplified the difference in the accessible hydrophobic surface area among isomers, directly translating geometric mismatches into measurable binding energy differences. DFT further proved that the asymmetric sinuous channels of Al-TCPB-Me_2 can provide the shape-matching effect to distinguish *p*X and *m*X.

Separation performance of the asymmetric sinuous channel in Al-MOFs

Following the confirmation of the asymmetric sinuous channel's capacity for tandem molecular sieving and shape-matching effects in isomer discrimination, the Al-TCPB-Me_2 material was implemented as a GC stationary phase for isomer separation. Comparative Al-TCPB coated columns and commercial HP-5 columns were tested to separate identical isomer mixtures (Fig. 4 and S10–S13).

The concentrations of coating material were controlled as 1 mg mL^{-1} (1 mL) for each column, respectively, to avoid their influence (Fig. S13). Experimental results revealed that the Al-TCPB-Me_2 column achieved baseline resolution for 10 groups of disubstituted benzene isomers and alkane compounds, demonstrating superior analytical scope and separation efficiency. For xylene isomer separation, R_s values reached 24.9 (*m*X/*p*X) and 31.1 (*o*X/*p*X), significantly outperforming state-of-the-art HP-5 columns and most of the reported stationary phases (Fig. 4c and Table S4). The elution sequence (*o*X > *m*X > *p*X) reflected differential molecular interactions. The *o*X's early elution aligned with the rapid kinetic diffusion through molecular sieves, while the delayed elution of *p*X corresponded to the enhanced thermodynamic binding through shape matching. This tandem mechanism facilitated consistent baseline separation across various disubstituted benzene isomers, confirming the strategic advantage of engineered sinuous channels in the synergistic size exclusion and molecular recognition for *ortho*-, *meta*-, and *para*-isomer differentiation (Fig. 4a and S11). The column also exhibited excellent operational and long-term stability, as confirmed by its consistent performance across multiple batches, repeated injections, thermal cycling, and seven-month storage (Fig. S14–S17).

The separation performance of Al-TCPB with straight channels was also evaluated. The Al-TCPB coated column baseline separated several isomers, such as xylene and ethyltoluene, although the separation performance was significantly lower than the Al-TCPB-Me_2 coated column. For example, the R_s values of *o*X/*p*X and *m*X/*p*X were 5.3 and 9.1, respectively (Table S4). Notably, the elution order of xylenes on Al-TCPB was *m*X > *o*X > *p*X, differing from that observed in Al-TCPB-Me_2. This elution sequence was consistent with the relative ΔH values, suggesting that the separation in Al-TCPB was primarily governed by shape-matching interactions without significant molecular sieving effects. The column efficiency of these two columns was measured by using *o*X as the target (Fig. S18). The column efficiency of the Al-TCPB coated column was 1895 plates/m, smaller than that of the Al-TCPB-Me_2 coated column (3289 plates/m, Table S5). When separating chlorotoluene isomers and dichlorobenzene isomers, Al-TCPB can separate *para*-isomers from others but cannot distinguish the *meta*- and *ortho*-isomers (Fig. 4b and S10). These comparative results conclusively validated the superior performance of the

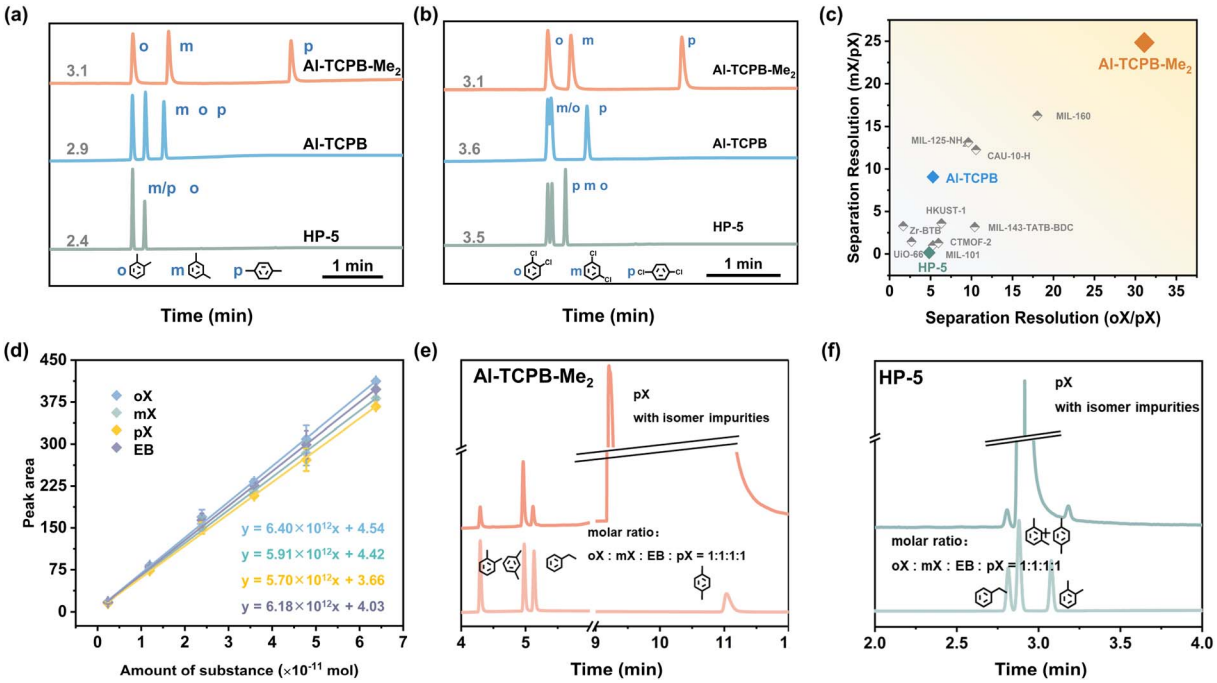

Fig. 4 The GC separation chromatograms of (a) xylene isomers and (b) dichlorobenzene isomers on HP-5, Al-TCPB, and Al-TCPB-Me_2 columns, respectively. (c) The isomer separation resolution of *m*X/*p*X and *o*X/*p*X on different MOF columns and the commercial column HP-5, respectively. (d) The standard curves of *o*X, *m*X, *p*X, and EB on the 30 m Al-TCPB-Me_2 column. (e) Gas chromatograms of *p*X with isomer impurities on the 30 m Al-TCPB-Me_2 coated column. All four isomers were totally separated from each other. (f) Gas chromatograms of *p*X with isomer impurities on the 30 m HP-5 column. The *m*X could not be separated from the main peak *p*X, while peak tailing affects the accurate quantification of *o*X.

asymmetric sinuous channel in Al-TCPB-Me_2 with a tandem separation mechanism.

Quantification of isomer impurities in a high quality sample

To assess the quantification ability of the Al-TCPB-Me_2 column, four xylene isomers (*o*X, *m*X, *p*X, and EB) were mixed in *n*-heptane at a 1 : 1 : 1 : 1 molar ratio. Their concentrations were adjusted by varying the volume of *n*-heptane. The solutions of each concentration were injected into the 30 meter Al-TCPB-Me_2 column under the same programmed heating conditions, respectively. Chromatograms showed baseline separation of all isomers with no interference in peak area integration (Fig. S19). Each isomer's calibration curve had a goodness of fit above 0.99 (Fig. 4d and Table S6). Detection limits (LODs, S/N = 3) were 2.59 ± 0.22 pg for *o*X, 3.11 ± 0.22 pg for *m*X, 15.39 ± 1.99 pg for *p*X, and 3.08 ± 0.13 pg for EB (Table S7). It is worth noting that the above LODs could be even lower with proper analytical strategies, such as sample preparation and mass spectrometry (MS) or MS/MS detectors. These results confirmed the Al-TCPB-Me_2 column's reliable quantification performance.

To further confirm the Al-TCPB-Me_2 column's ability to quantify trace isomeric impurities, a real high-quality *p*X sample was analyzed. The three impurities (*o*X, *m*X, and EB) eluted between 4 and 6 minutes, while pure *p*X eluted after 12 minutes, ensuring the main *p*X peak broadening and trailing did not interfere with impurity detection (Fig. 4e). Using calibration curves, the impurities of *o*X, *m*X, and EB were measured as 200 ± 30 ppm, 800 ± 10 ppm, and 200 ± 20 ppm (w/w), respectively (Table S8), in the pure *p*X sample. It is worth noting that the values did not align with the LODs for the Al-TCPB-Me_2 column. Theoretically, impurities as low as 6.3 ppm could be quantified, which is suitable for the analysis of ultrahigh-grade samples, such as electronic chemicals (>99.9994% w/w). For comparison, the conventional HP-5 column was used to analyze the same *p*X sample, but it failed to quantify impurities due to poor separation and interference from *p*X peak tailing (Fig. 4f and S20). This validates the Al-TCPB-Me_2 column's superior performance in trace isomer impurity quantification.

Conclusions

In summary, we demonstrated the successful development of Al-TCPB-Me_2 with asymmetric sinuous one-dimensional channels as a high-performance GC stationary phase for resolving persistent challenges in *p*X trace isomer separation and qualification. By synergistically integrating molecular sieving and shape matching mechanisms, the material's unique asymmetric sinuous channel architecture enabled exclusion of *o*X through size selectivity while leveraging asymmetric binding interactions to differentiate *p*X and *m*X. The separation mechanism was proved by both thermodynamic interaction and kinetic diffusion investigation. The Al-TCPB-Me_2 column achieved exceptional separation resolutions and impurity quantification down to 200 ppm in a high-purity sample, significantly surpassing conventional columns. The comparison material Al-TCPB with straight channels showed lower separation resolution of all

isomer mixtures than Al-TCPB-Me_2, emphasizing the critical role of sinuous geometry in achieving the high performance. These findings advanced the precision of industrial xylene isomer analysis and established a versatile design strategy for engineering advanced separation materials targeting complex multi-component systems with near-identical physicochemical properties.

Author contributions

Z.-Y. G. conceived the idea and supervised the research. M. X., X. Y. F. and S.-S. M. performed the synthesis, characterization, and GC experiments and discussed the results. S. R. G. and Y. W. performed the DFT simulation. Z.-Y. G. and M. X. discussed the experimental data and wrote the paper. All authors have approved the final version of the manuscript.

Conflicts of interest

There are no conflicts to declare.

Data availability

The data supporting this article have been included as part of the supplementary information (SI). Supplementary information is available. See DOI: https://doi.org/10.1039/d5sc07611k.

Acknowledgements

This work was supported by the National Natural Science Foundation of China (22374077 and 22474059) and the Priority Academic Program Development of Jiangsu Higher Education Institutions. This work was carried out with the support of BL17B1 at the Shanghai Synchrotron Radiation Facility (proposal 2023-NFPS-PT-500772).

Notes and references

1 Y. Liu, C. Wang, Q. Yang, Q. Ren and Z. Bao, *Coord. Chem. Rev.*, 2025, **523**, 216229.
2 M. Xu, W.-Q. Tang, S.-S. Meng and Z.-Y. Gu, *Chem. Soc. Rev.*, 2025, **54**, 1613–1633.
3 M. Rahmani, C. R. M. O. Matos, S.-Q. Wang, A. A. Bezrukov, A. C. Eaby, D. Sensharma, Y. Hjiej-Andaloussi, M. Vandichel and M. J. Zaworotko, *J. Am. Chem. Soc.*, 2023, **145**, 27316–27324.
4 L. Yu, J. Zhang, S. Ullah, J. Yao, H. Luo, J. Huang, Q. Xia, T. Thonhauser, J. Li and H. Wang, *Angew. Chem., Int. Ed.*, 2023, **62**, e202310672.
5 N. Zhu, J. Wu and D. Zhao, *ACS Nano*, 2025, **19**, 2029–2046.
6 Y.-J. Zhao, W.-Q. Tang, X.-W. Wang, H.-F. Zhao, Z.-Y. Gu, Q. Yang and D. Liu, *Chem. Sci.*, 2022, **13**, 11896–11903.
7 S. Halder, Z. Xie, M. H. Nantz and X.-A. Fu, *J. Chromatogr. A*, 2022, **1673**, 463083.
8 B. Chen, C. Liang, J. Yang, D. S. Contreras, Y. L. Clancy, E. B. Lobkovsky, O. M. Yaghi and S. Dai, *Angew. Chem., Int. Ed.*, 2006, **45**, 1390–1393.
9 J. Wang, X. Lu, Z. Zhang, R. Gao, C. Pei and H. Wang, *J. Chromatogr. A*, 2024, **1718**, 464718.
10 M. Chang, Z. Wang, R. Wang, M. Liu, Y. Wang and D. Liu, *Angew. Chem., Int. Ed.*, 2025, **64**, e202515496.
11 Z.-H. Guo, L.-Q. Yang, Q.-G. Zhai, G.-P. Yang and Y.-Y. Wang, *Angew. Chem., Int. Ed.*, 2025, **64**, e202519278.
12 C.-X. Chen, X. Cui, Y.-Y. Xiong, P. C. Lan, K. Tan, Z.-W. Wei, Z. Niu, C. Shan, L. Yang, S. Ma and C.-Y. Su, *Nat. Synth.*, 2025, DOI: 10.1038/s44160-025-00911-7.
13 Y. Wang, N.-Y. Huang, X.-W. Zhang, H. He, R.-K. Huang, Z.-M. Ye, Y. Li, D.-D. Zhou, P.-Q. Liao, X.-M. Chen and J.-P. Zhang, *Angew. Chem., Int. Ed.*, 2019, **58**, 7692–7696.
14 Q. Ding, Z. Zhang, C. Yu, P. Zhang, J. Wang, X. Cui, C.-H. He, S. Deng and H. Xing, *Sci. Adv.*, 2020, **6**, eaaz4322.
15 S. Lee, A. Sharma, J. H. Lee, J. Lim, S. K. Min, H. Chun and M. S. Lah, *Angew. Chem., Int. Ed.*, 2025, **64**, e202512244.
16 S. A. Mohamed, R. Zheng, N. Zhu, D. Zhao and J. Jiang, *J. Am. Chem. Soc.*, 2025, **147**, 12251–12262.
17 L. Li, L. Guo, D. H. Olson, S. Xian, Z. Zhang, Q. Yang, K. Wu, Y. Yang, Z. Bao, Q. Ren and J. Li, *Science*, 2022, **377**, 335–339.
18 X.-J. Xie, H. Zeng, Y.-L. Huang, Y. Wang, Q.-Y. Cao, W. Lu and D. Li, *Chem*, 2025, **11**, 102339.
19 Q. Liu, Y. Miao, L. F. Villalobos, S. Li, H.-Y. Chi, C. Chen, M. T. Vahdat, S. Song, D. J. Babu, J. Hao, Y. Han, M. Tsapatsis and K. V. Agrawal, *Nat. Mater.*, 2023, **22**, 1387–1393.
20 X. Wu, X. Tian, W. Zhang, X. Peng, S. Zhou, P. J. S. Buenconsejo, Y. Li, S. Xiao, J. Tao, M. Zhang and H. Yuan, *Angew. Chem., Int. Ed.*, 2024, **63**, e202410411.
21 X. Zhang, X. Tian, N. Wu, S. Zhao, Y. Qin, F. Pan, S. Yue, X. Ma, J. Qiao, W. Xu, W. Liu, J. Liu, M. Zhao, K. Ostrikov and Z. Zeng, *Sci. Adv.*, 2024, **10**, eadl6498.
22 H. Wang, Y. Liu and J. Li, *Adv. Mater.*, 2020, **32**, 2002603.
23 M. Xu, S.-S. Meng, P. Cai, W.-Q. Tang, Y.-D. Yin, J. A. Powell, H.-C. Zhou and Z.-Y. Gu, *Chem. Sci.*, 2021, **12**, 4104–4110.
24 R. Lyndon, Y. Wang, I. M. Walton, Y. Ma, Y. Liu, Z. Yu, G. Zhu, S. Berens, Y.-S. Chen, S. G. Wang, S. Vasenkov, D. S. Sholl, K. S. Walton, S. H. Pang and R. P. Lively, *Chem. Commun.*, 2022, **58**, 12305–12308.
25 Q. Wang, Y. Li, Z. Qiu, D. Zhou, L. Yang, X. Suo, X. Cui and H. Xing, *Angew. Chem., Int. Ed.*, 2024, **63**, e202408817.
26 X. Cui, Z. Niu, C. Shan, L. Yang, J. Hu, Q. Wang, P. C. Lan, Y. Li, L. Wojtas, S. Ma and H. Xing, *Nat. Commun.*, 2020, **11**, 5456.
27 J. Li, B. Sheng, R. Chen, H. Wu, W. Zhou, F. Zheng, B. Liu, Q. Yang, Z. Zhang, Y. Yang, Q. Ren and Z. Bao, *Adv. Mater.*, 2025, **37**, 2413506.
28 Z. Chu, J. Li, F. Chen, Y. Cao, L. Chen, F. Zhou, H. Ma, Q. Yang, Z. Zhang, K. Qiao, Q. Ren and Z. Bao, *ACS Cent. Sci.*, 2024, **10**, 1861–1870.
29 H. Yuan, K. Li, D. Shi, H. Yang, X. Yu, W. Fan, P. J. S. Buenconsejo and D. Zhao, *Adv. Mater.*, 2023, **35**, 2211859.
30 H. Zeng, M. Xie, T. Wang, R.-J. Wei, X.-J. Xie, Y. Zhao, W. Lu and D. Li, *Nature*, 2021, **595**, 542–548.
31 L. Li, Z. Yang, Q. Wang, L. Yang, X. Suo, X. Cui and H. Xing, *Small*, 2025, **21**, 2412724.

32 M.-Y. Zhou, X.-W. Zhang, H. Yi, Z.-S. Wang, D.-D. Zhou, R.-B. Lin, J.-P. Zhang and X.-M. Chen, *J. Am. Chem. Soc.*, 2024, **146**, 12969–12975.
33 Z.-J. Jiang, Y. Wang, D. Luo, R.-J. Wei, W. Lu and D. Li, *Angew. Chem., Int. Ed.*, 2024, **63**, e202403209.
34 X.-W. Zhang, H. He, Y.-W. Gan, Y. Wang, N.-Y. Huang, P.-Q. Liao, J.-P. Zhang and X.-M. Chen, *Angew. Chem., Int. Ed.*, 2024, **63**, e202317648.
35 F. Xie, L. Chen, E. M. Cedeño Morales, S. Ullah, Y. Fu, T. Thonhauser, K. Tan, Z. Bao and J. Li, *Nat. Commun.*, 2024, **15**, 2240.
36 S. Grimme, S. Ehrlich and L. Goerigk, *J. Comput. Chem.*, 2011, **32**, 1456–1465.
37 G. Kresse and J. Furthmüller, *Phys. Rev. B:Condens. Matter Mater. Phys.*, 1996, **54**, 11169–11186.
38 M. Krüger, R. Siegel, A. Dreischarf, H. Reinsch, J. Senker and N. Stock, *Micropor. Mesopor. Mat.*, 2015, **216**, 27–35.
39 G. M. R. Dontireddy, S. P. Suman, J. L. Merino-Gardea, A. H. Javed, J. Wang, T. Chen, S. Kampouri and H. Banda, *J. Mater. Chem. A*, 2025, **13**, 8734–8741.
40 L. Yan, H.-T. Zheng, L. Song, Z.-W. Wei, J.-J. Jiang and C.-Y. Su, *Chem. Eng. J.*, 2023, **472**, 145145.
41 A. Gładysiak, A.-Y. Song, R. Vismara, M. Waite, N. M. Alghoraibi, A. H. Alahmed, M. Younes, H. Huang, J. A. Reimer and K. C. Stylianou, *JACS Au*, 2024, **4**, 4527–4536.
42 M. Lammert, H. Reinsch, C. A. Murray, M. T. Wharmby, H. Terraschke and N. Stock, *Dalton Trans.*, 2016, **45**, 18822–18826.
43 Y. Yang, P. Bai and X. Guo, *Ind. Eng. Chem. Res.*, 2017, **56**, 14725–14753.